scientific reports

Check for updates

OPEN

Stress–strain curve predictions by crystal plasticity simulations and machine learning

Dmitry S. Bulgarevich✉ & Makoto Watanabe

The stress–strain curve (SSC) prediction for additively manufactured as-build metal materials with laser powder bed fusion (LPBF) is a lengthy and tedious process. It involves the sophisticated representative volume element (RVE) reconstruction of complex experimental microstructures for subsequent state-of-the-art crystal plasticity simulations with hyperparameter tunings in the appropriate physical model. However, even with a well-fitted model, simulations with different RVEs or temperatures, for example, are too time-consuming and computationally intensive. In recent years, several attempts were directed towards the SSC predictions with machine learning (ML) tools to speed up this process. Mainly, the artificial neural networks (ANN) were reported so far for this purpose. Here, we present our version to predict the temperature dependence of SSCs for LPBF fabricated industrially important Hastelloy X with various ML methods. Compared to previously reported studies on this matter with direct link between the microstructures and SSCs, we directly link only experimental conditions and predicted SSCs, which could be more preferable for some application scenarios discussed below. It was found that due to the structure and "small" size of our training dataset, the decision tree-based ML regressors worked better than other popular ML methods.

In our already published report, we discussed in details the challenges, literature survey and our developed workflow to predict accurately the SSCs of LPBF manufactured materials from experimental EBSD data on microstructures with complex RVE reconstruction and corresponding CP simulations[1]. However, the simulation time for a single SSC prediction was still in hours, if not days, even on modern laboratory Workstation, not to mention the time for RVE reconstruction. Note that the whole sophisticated analysis/simulation process may not be suitable/appropriate for some analytical laboratories which are interesting for routine SSC predictions of LPBF materials. For such scenarios, the well-trained ML regressor is desirable to predict the SSC within a few seconds or less. In other words, once multiple RVE reconstructions and CP simulations were used to construct the training dataset with corresponding SSCs and ML regression model was built on such dataset, then SSC predictions within reasonable experimental parameter constrains can be done in a very short time even without prior user knowledge on ML model, RVE reconstruction and CP simulation details.

For example, the ANN and linear regressors (LR) were used to predict the SSCs of low-carbon steels form experimental microstructure characteristics. To quantify the ferrite-pearlite microstructures, the two-point correlation was used with reduced dimensionality by principal component analysis (PCA)[2]. The training dataset for ML was constructed with such PCA selected components and low-cycle fatigue SSCs from 2D crystal plasticity-based finite element model (CPFEM) on reconstructed RVE slices. The good agreements between experimental and ML results were achieved especially with ANN. The convolutional neural network (CNN) was also reported for SSC predictions beyond the elastic limit for binary composite materials by using the training dataset consisting of SSCs and soft/stiff block microstructures with PCA reduced dimensionality[3]. In another work, the prediction of SSCs of ferrite-martensite dual-phase steels was also studied by ANN, but on experimental SSCs in small training dataset with Bayesian inference for appropriate attribute selection from the pool of volume fraction, micro-hardness, void of martensite phase and micro-hardness of ferrite phase, i.e. from the combination of experimental material microstructure and mechanical properties[4,5]. In addition, the high quality SSC predictions with ANN on training dataset with SSCs and microstructure texture from CPFEM simulations were reported for polycrystalline metals[6]. Similar approach, though without experimental verifications, was also reported to build the ML ANN model in order to predict the temperature-dependent SSCs by using the training dataset from CPFEM simulated SSCs on automatically generated RVEs with different microstructures for some typical soft/hard phase material[7]. Moreover, the support vector machine (SVM) and ANN were applied to predict the SSCs of crystals from simulated mapping of discrete dislocations[8].

National Institute for Materials Science, 1-2-1 Sengen, Tsukuba, Ibaraki 305-0047, Japan. ✉email: bulgarevich.dmitry@nims.go.jp

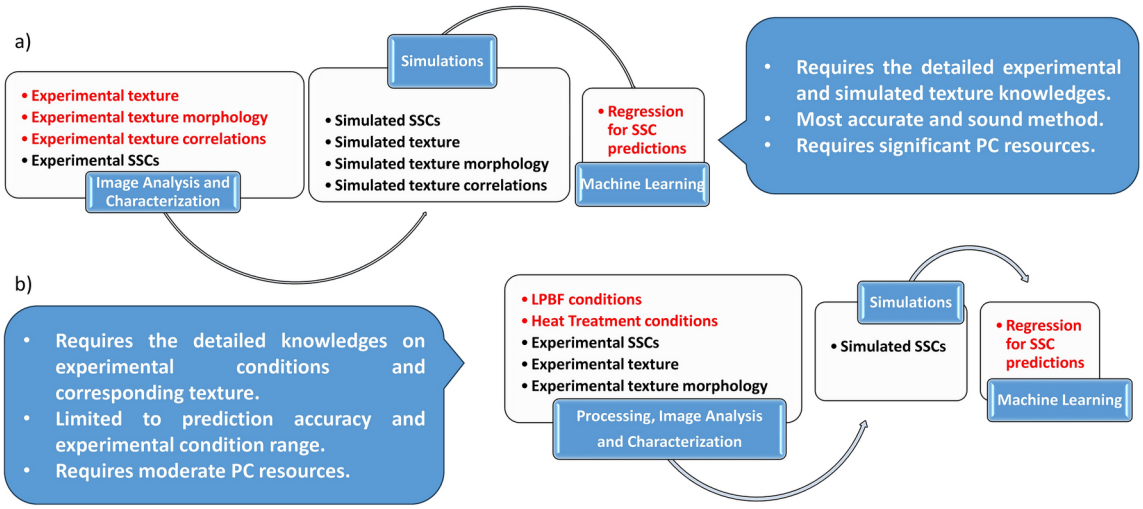

Fig. 1. General attributes for SSC predictions with ML: (**a**) in literature reported to date, the direct links of the microstructures with predicted SSCs were typically reported, i.e. the user always needs the detailed microstructure knowledge for SSC predictions (red color text); (**b**) in current study, we directly link the experimental conditions with predicted SSCs, i.e. ones ML regression model is built, only the knowledge on experimental conditions is required to predict the SSCs (red color text).

Element	Ni	Fe	C	W	Co	Cr	Mo	Si	Mn	P	S
Composition	Bal	18.1	0.06	0.7	1.6	22.1	9.0	0.1	0.0	0.005	0.003

Table 1. Hastelloy X powder composition.

Recently, the Gaussian process (GP) regression, ANN and boosted trees (BST) in predicting SSCs for Al6061-T6 precipitation-hardened aluminum alloy were reported[9]. The training and testing were conducted on 70 and 30% split dataset with SSC at 25, 100, 200, and 300 °C, respectively. Though, the results indicated that the NN and GP models were capable to forecast the SSC from test dataset and outperformed the BST model in terms of prediction accuracy, the validation on unseen data for intermediate temperatures were not conducted to exclude the possible overfitting.

Note that literature on this subject is very limited especially regarding to additively manufactured materials typically having the very complex microstructures. We are aware of only a single comprehensive work on this subject for stainless steels with direct link of CPFEM modeled SSCs and microstructure images (with phase composition and crystallographic information) by deep neural network (DNN)[10]. Also, as it can be seen from above examples, the ML modes were based on ANN regressors with training datasets consisting of microstructure, mechanical property or a mixture of both attributes. It seems that attempts to link directly the LPBF experimental parameters and predicted SSCs were not reported yet. In this regard, the appropriate ML regressor choice may depend on training dataset structure and its size. Therefore, this is the interesting and important task for the current investigation in order to speed up the SSC predictions for such materials. See Fig. 1a,b with summaries on reported and current approaches for SSC predictions, respectively.

Material and methods

Three different Hastelloy X cylindrical specimens were fabricated on SLM280HL from SLM Solutions Group AG (Lübeck) with different laser power (P), scanning speed (v) and energy density (E) at 1064 nm wavelength, 80 µm spot diameter (Gaussian profile), and 100 µm scan pitch: E50P500v3333, E80P500v2083 and E140P300v714 samples, where P, v and E are in W, mm/s and J/mm^3, respectively. The stripe scan pattern was applied with 100 µm scan pitch, and the scanning direction was rotated 90° every layer. The Hastelloy X powder (AMPERPRINT 0228.074; Höganäs AB), a Ni-based superalloy with a particle size of 15–45 µm, was used with chemical composition summarized in Table 1. The powder layer thickness was about 30 µm. The cylindrical samples with a diameter of 10 mm and a height of 8 mm were built with a support length of 3 mm from a stainless steel base plate. The LPBF samples were analyzed in the XY and XZ planes by a scanning electron microscope (SEM, JSM-7200F; JEOL Corp.) with an electron backscatter diffraction (EBSD).

The data pipeline and simulations in all details were provided in our previous publication[1]. Here, we used the Dream3D 6.5.150 and DAMASK 3.0 open-source packages[11–13] for RVE reconstruction and CP modeling, respectively. The color maps from simulations were visualized with ParaView 5.9.0-RC2[14]. All ML studies were conducted on open-source WEKA 3.8.6 software package with a collection of ML algorithms[15]. The POWER

MASTER Vision S5165 Workstation (System Works) with two Xeon Gold 6226R CPUs and 384 GB ECC RAM was used in this research.

Results and discussion

The RVE reconstructions and CP-simulated SSCs

Figure 2a shows the experimental EBSD cross-section maps in XY and XZ planes for Hastelloy X samples and pole figures with crystallographic information for one of them. With laser surface energy increase, the formation of the columnar core microstructures is observed from random to square lattice grain distribution in the raw of E50P500v3333, E80P500v2083 and E140P300v714 samples. The lattice pitch in E80P500v2083 and E140P300v714 corresponds to the laser scanning pattern. The corresponding RVEs reconstructed from such EBSD data by published procedure[1] are displayed in Fig. 2b,c. Figure 2b demonstrates in more details the various color mappings with different "phases" (microstructure types), grains and crystal orientations in RVE-1. The Lambert pole figures for RVE-1 are also shown to demonstrate the good correspondence between experimental and reconstructed data as required from Fig. 1a,b. Here it must be stressed that RVEs on Fig. 2 are not the visually identical copies of experimental samples, but statistical ones in terms of microstructure properties. The statistical parameters for Columnar Core and matrix (other) microstructure types were extracted from experimental EBSD data and used to reconstruct these RVEs in Dream3D. They are listed in Table 2 with their parameter meanings and extraction procedures given in Ref.[1]: the log-normal-shape probability density function (PDF_{L-N}) of grain size, the beta-function-shape probability density function (PDF_B) of grain shape, the axis orientation distribution function (ODF) of grains, the crystal ODF of grains and the radial distribution function (RDF) of Columnar Core grains. The experimental (f_V^{exp}) and reconstructed (f_V) microstructure volume fractions are also given in Table 2. It should be noted that precipitate microstructures (microstructures embedded into columnar cores) were introduced to have some experimentally observed imperfections in columnar cores for E80P500v2083 and E140P300v714 samples.

The CP simulations of tensile tests were also conducted as described in details in Ref.[1] by using DAMASK Spectral Solver and phenomenological model for plasticity[16]:

$$\tau^{\alpha} = S : (m^{\alpha} \otimes n^{\alpha}) \tag{1}$$

$$\dot{\gamma}^{\alpha} = \dot{\gamma}_0 \left| \frac{\tau^{\alpha}}{\tau_0^{\alpha}} \right|^{w} \operatorname{sgn}(\tau^{\alpha}) \tag{2}$$

$$\dot{\tau}_0^{\alpha} = \sum_{\alpha'=1}^{N_s} h_{\alpha\alpha'} \left| \dot{\gamma}^{\alpha'} \right| \tag{3}$$

$$h_{\alpha\alpha'} = q_{\alpha\alpha'} \left[h_0 \left(1 - \frac{\tau_0^{\alpha}}{\tau_{\infty}} \right)^{a} \right] \tag{4}$$

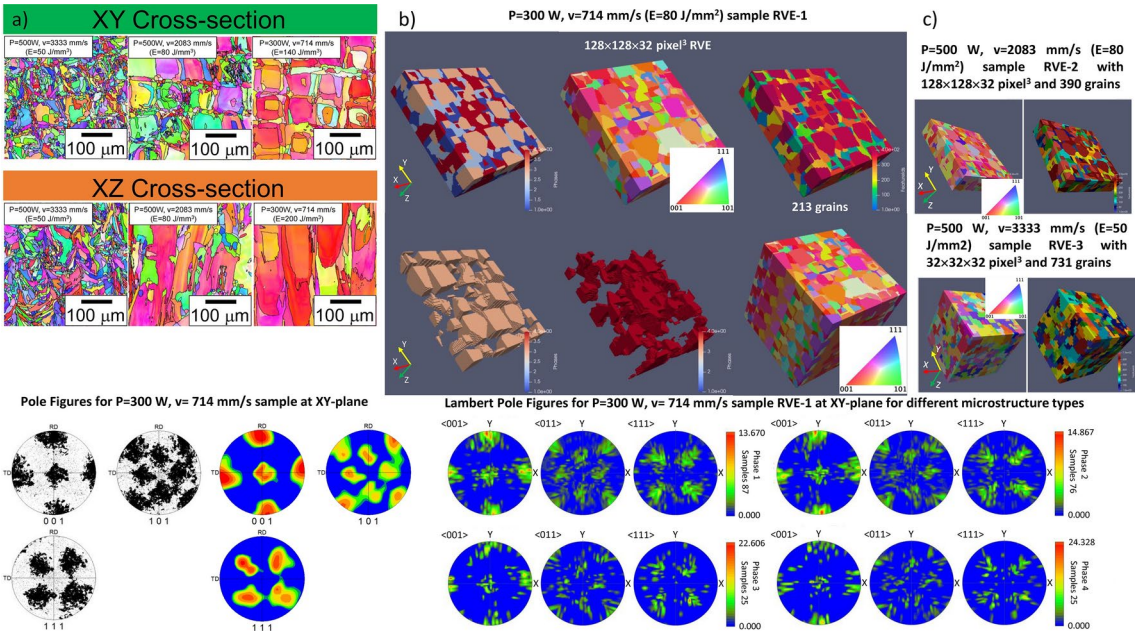

Fig. 2. Experimental EBSD data in (**a**) and reconstructed RVEs in (**b**) and (**c**). In (**b**) and (**c**), the phases in color bars are the microstructure types (super ellipsoid, cube octahedron and their ODF variables); the features in color bars are the individual grains.

Microstructure	Sample (f_V^{exp})	f_V	Shape type	PDF_{L-N}						PDF_B		Aspect ratio		Axis ODF			RDF	Crystal ODF		
				μ	σ	BSS	Min	Max	ESB (av, min, max)	α	β	b/a	c/a	Euler angles	σ	w		Euler angles	σ	w
Columnar cores	E140P300v714 (0.543)	0.233 (precipitate) 0.284 (primary)	Cube Octahedron	4.75 4.74	10^{-3} 0.112	1 10	0.1 5	0.1 0	116, 116, 116 115, 65, 115	140	42	0.45	0.45	(0,90,90)	1	50,000	Square lattice (centroids)	Directly sampled from EBSD data table		
	E80P500v2083 (0.342)	0.172 (precipitate) 0.148 (primary)	Cube Octahedron	4.72 4.72	10^{-3} 0.112	1 10	0.1 5	0.1 0	112, 112, 112 112, 64, 112	140	42	0.48	0.48	(0,90,90)	1	50,000	Square lattice (centroids)	Directly sampled from EBSD data table		
	E50P500v3333 (0)	–	–	–	–	–	–	–	–	–	–	–	–	–	–	–	–	–		
Matrix	E140P300v714 (0.457)	0.258 (primary) 0.225 (primary)	Cube Octahedron	3.6	0.34	20	2	2.5	39, 19, 86	140	42	0.71	0.28	(90, −90, −90) (0, 90, 90)	1	50,000	–	Directly sampled from EBSD data table		
	E80P500v2083 (0.658)	0.346 (primary) 0.334 (primary)	Cube Octahedron	3.57	0.34	20	2	2.5	38, 18, 83	140	42	0.84	0.34	(90, −90, −90) (0, 90, 90)	1	50,000	–	Directly sampled from EBSD data table		
	E50P500v3333 (1)	1 (primary)	Super Ellipsoid	2.43	0.34	20	2.2	3.1	12, 5, 33	10	1.7	0.80	0.33	(90, −90, −90	2	500	–	Directly sampled from EBSD data table		

Table 2. Parameters to define the microstructures in Dream3D for RVE reconstruction from Fig. 2 and EBSD data tables. The meaning of all statistical parameters are given in Ref.[1].

with variables and parameters from Eqs. (1–4) listed in Table 3 and with additional ones used in DAMASK Spectral Solver. The temperature dependence of elastic stiffness constants was taken from literature data[17]. The mixed boundary conditions for uniaxial tension along x–, y– and z– axes are described by Eqs. (5–7), respectively:

$$\dot{\bar{F}} = \begin{bmatrix} 10^{-3} & 0 & 0 \\ 0 & * & 0 \\ 0 & 0 & * \end{bmatrix} \mathrm{s}^{-1} \quad \text{and} \quad \bar{P} = \begin{bmatrix} * & * & * \\ * & 0 & * \\ * & * & 0 \end{bmatrix} \mathrm{Pa} \tag{5}$$

$$\dot{\bar{F}} = \begin{bmatrix} * & 0 & 0 \\ 0 & 10^{-3} & 0 \\ 0 & 0 & * \end{bmatrix} \mathrm{s}^{-1} \quad \text{and} \quad \bar{P} = \begin{bmatrix} 0 & * & * \\ * & * & * \\ * & * & 0 \end{bmatrix} \mathrm{Pa} \tag{6}$$

$$\dot{\bar{F}} = \begin{bmatrix} * & 0 & 0 \\ 0 & * & 0 \\ 0 & 0 & 10^{-3} \end{bmatrix} \mathrm{s}^{-1} \quad \text{and} \quad \bar{P} = \begin{bmatrix} 0 & * & * \\ * & 0 & * \\ * & * & * \end{bmatrix} \mathrm{Pa} \tag{7}$$

where $\dot{\bar{F}}$ and $\bar{P}$ are the deformation gradient rate and Piola–Kirchhoff stress tensors, respectively, with undefined components indicated by asterisks. They satisfy the mutual exclusiveness of $\dot{\bar{F}}$ and $\bar{P}$ as well as prevent rotation (undefined $\bar{P}$ off-diagonal components)[18] Table 2. Parameters to define the microstructures in Dream3D for RVE reconstruction from Fig. 2 and EBSD data tables. The meaning of all statistical parameters are given in Ref.[1].

Figure 3 shows the experimental and several simulated SSCs with best manually fitted parameters a, w, $\dot{\gamma}_0$, τ_0^α, τ_∞, and h_0 from phenomenological model for CP. Other parameters are the same as in Table 3. The simulated SSCs are plotted in terms of the "nominal" or"engineering" (force divided by the original sectional area) stress and nominal strain. The nominal stress (σ_N) or strain (ε_N) corresponds to the averaged tensor component along x–, y– or z– axis for RVE from transpose of the DAMASK-simulated Piola–Kirchhoff stress tensor, $\sigma_N = \bar{P}^T$, or from the true strain tensor (ε_T), $\varepsilon_N = e^{\varepsilon_T} - 1$, respectively[13]. It takes ~ 21 h per simulation and subsequent post-processing on 32-CPU cores with 1480 simulation steps per SSC. In Fig. 3a, the RVE-1 was used with tension along z–axis for fitting of the parameters in CP model to get the best correspondence with experimental SSC. It was achieved with linear isotropic slip hardening process ($a \approx 0$) and nonlinear strain rate sensitivity ($w > 1$): a= 0.01, w= 80, $\dot{\gamma}_0$ = 0.001, τ_0^α= 235 MPa, τ_∞= 700 MPa, and h_0= 240 MPa. Due to the discontinuous columnar or/and grain microstructures (see Fig. 2b), there was little anisotropy between the simulated SSCs with loads along x–, y– and z– axes which reflects the inconsistency of experimental results in this respect. Then, such fitted parameters were used with other RVEs. However, is this case, the correspondence between experimental and simulated SSCs for other RVEs was poor (see Fig. 3a).

To deal with this problem, the parameters in CP simulations were well-fitted for each RVE on several corresponding experimental SSC along single axis. Then, such parameters were applied to other load-axis

Value	Definition	Hastelloy X	
Variable	α	Slip system	
	τ^α	Resolved shear stress (analogous to Schmid's law)	
	m^α	Vector in slip/shear direction	
	n^α	Vector along plane normal of the respective slip system	
	$\dot{\gamma}^\alpha$	Plastic shear rate on each slip system	
	$\dot{\tau}_0^\alpha$	Hardening/resistance behavior/kinetics of a slip system	
	$h_{\alpha\alpha\prime}$	Hardening matrix	
Parameter	a	Slip hardening	0.01
	w	Strain rate sensitivity	80
	$q_{\alpha\alpha\prime}$	Latent hardening for (coplanar) and [otherwise] slips	(1, 1), [1.4, 1.4, 1.4, 1.4]
	$\dot{\gamma}_0$	Reference shear rate, s^{-1}	0.001
	τ_0^α	Initial slip resistance to plastic flow, MPa	247 at RT and Eqs. 11 and 12 from Ref.[17]
	τ_∞	Saturation stress or resistance to plastic flow, MPa	700 at RT and Eqs. 11 and 12 from Ref.[17]
	h_0	Slip hardening, MPa	240
	C_{11}	Elastic stiffness constants from elasticity matrix, GPa	Equation 10 from Ref.[17]
	C_{12}		
	C_{14}		
	$Latt\_str$	Lattice structure	fcc
	N_s	Number of slip systems	12

Table 3. Symbols, meanings and values of parameters in phenomenological model for crystal plasticity used in this study for simulated temperature dependence of SSCs. The τ_0^α and τ_∞ values at room temperature (RT) for Hastelloy X correspond to the averaged ones from Fig. 3b. See text for more details.

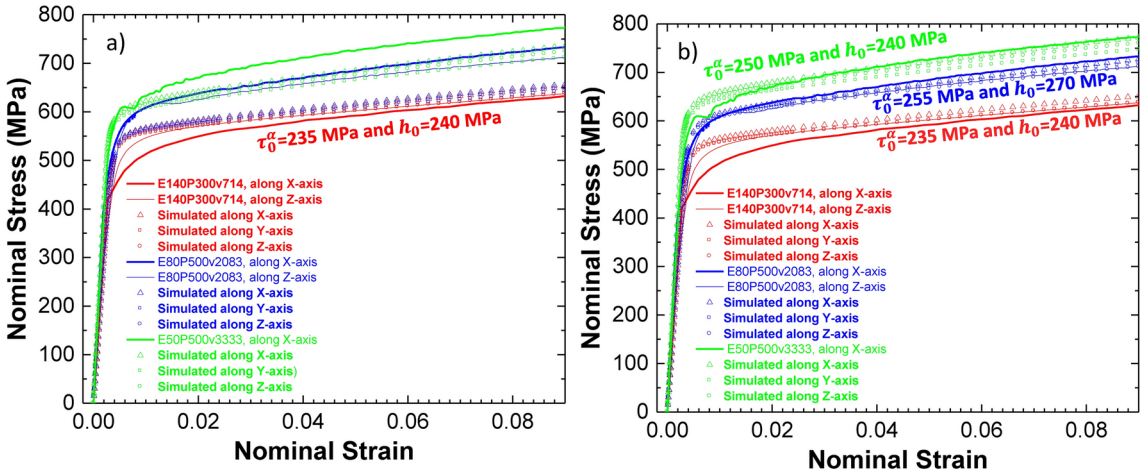

Fig. 3. Results of DAMASK simulation fittings with phenomenological model for crystal plasticity to experimental SSCs: (**a**) the model parameters for predicted SSCs were fitted on single experimental SSC along z-axis with reconstructed RVE-1 and applied without change to other RVEs, (**b**) the model parameters for predicted SSCs were fitted on each experimental SSC along single x- or z- axis and applied to other load axes. Note that in (**a**) and (**b**), the models are different only by two τ_0^α and h_0 kinematic hardening parameter values. See text for more details.

Sample	Load, XYZ axes	Training and testing temperature, °C																
		25	50	100	150	200	250	300	350	400	450	500	550	600	650	700	750	800
		Simulated (sim) and Machine Learned (ml) 0.2% Proof Stress, MPa																
E140P300v714	X_{sim}	570	557	534	**514**	498	**483**	471	**458**	448	**438**	429	**421**	414	**406**	400	**393**	387
	X_{ml}	565	554	531	**513**	499	**486**	471	**458**	445	**443**	430	**428**	415	**409**	399	**395**	385
	Y_{sim}	563	549	527	**507**	491	**476**	464	**452**	441	**432**	423	**415**	409	**401**	394	**387**	381
	Y_{ml}	557	546	524	**505**	492	**479**	465	**446**	438	**431**	423	**416**	408	**399**	392	**385**	380
	Z_{sim}	560	547	525	**505**	490	**474**	463	**450**	440	**431**	421	**414**	407	**399**	393	**386**	377
	Z_{ml}	553	546	523	**505**	491	**478**	464	**445**	437	**430**	422	**414**	407	**398**	391	**384**	428
E50P500v3333	X_{sim}	627	612	588		548		518		492		472		457		441		423
	X_{ml}	621	609	585	**565**	549	**533**	517		492		474		457		440		417
	Y_{sim}	611	597	573		534		505		480		460		445		430		
	Y_{ml}																	
	Z_{sim}	620	604	580		541		511		486		466		451		435		422
	Z_{ml}																	

Table 4. Comparison/validation of 0.2% proof stress for ML predicted SSCs with CP simulated ones. The plain and bold font numbers are from training and testing datasets, respectively.

simulations. The results are sown in Fig. 3b. In this case, the good fit can be achieved in each case by varying just two τ_0^α and h_0 kinematic hardening parameter values as indicated in Fig. 3b,i,e. by initial critical resolved shear stress (CRSS) for onset of plastic deformations and by initial increase in the yield strength of the material due to dislocation interactions, respectively. In principle, all CP model parameters should be the same for same material even with different microstructures. However, some SSC scattering for same material is expected and often observed experimentally due to the possible inhomogeneous defects in LPBF samples. This can be mitigated by statistical averaging of experimental SSCs and by including of the defect microstructures into RVEs, but such averaging is a very time consuming process and DAMASK Spectral Solver can struggle with convergence as it was discussed in Ref.[1]. Instead, the averaged values of CP model parameters were found from fitting of simulated SSCs with different RVEs on corresponding experimental SSCs. This set of parameters for Hastelloy X is listed in Table 3 and is used in training dataset construction with temperature dependent SSC for ML regression. The training and testing dataset structures with simulated SSCs can be understood from Table 4 (0.2% proof stress will be discussed at the end of this sub-section). Since at this stage we were mainly interested in the possibility of ML application for SSC predictions, only the perfect correspondence of simulated and ML SSCs was the main priority for the proof of principle.

The ML regression for SSC predictions from CP simulated SSCs

Figure 4a displays the temperature dependent SSCs simulated with RVE-1 and RVE-3 as two limiting cases with regularly or randomly distributed/oriented grains, respectively. In Fig. 4a more details on constructed training dataset are given in terms of used attributes for stress prediction: strain, temperature, laser power, laser scan velocity, and load direction. In this dataset, there are 120 stress/strain data points per SSC, 10 temperatures (50, 100, 200, 300, 400, 500, 600, 700 and 800 °C), 2 numerical data points for laser power (300 and 500 W) and laser scan velocity (714 and 3333 mm/s), and 3 numerical data points for load direction ($x \rightarrow 1$, $y \rightarrow 2$ and $z \rightarrow 3$). Note that all attributes in our training dataset for stress estimation are independent ones. Therefore, no attribute selections were additionally performed with ML tools in this study.

In WEKA there are over 200 ML tools, but only 17 are suitable as regressors and handful ones support the numerical class. The most popular ones were tested and presented here. Others are meta-regressors, which typically include these 17 ones as a hyperparameter or some attribute selection method. The latter one is not important for our training dataset with only 5 truly independent attributes. Figure 5 demonstrates the performance of several popular ML regressors trained with tenfold cross-validation on training dataset from Fig. 4: the isotonic regression (IR), GP, sequential minimal optimization (SMO) algorithm used to solve the quadratic programming problem that arises during the training of SVM, multilayer perceptron (MLP), and random forest (RF) from WEKA implementations[15] in their default configurations (except 500 trees in RF and PolyKernel with exponent 2 for SMO and GP). Apparently, the best correspondence between predicted and actual stress values from training dataset were observed with RF as shown with linear fit details in Fig. 5a. Figure 5b shows the prediction results with RF in more details. Although the almost perfect correspondence between predicted and simulated SSCs were observed with training dataset, the predictions for unseen SSCs, for example at 150 °C, was very poor even with RF trained on 1000 trees: the RF predicted SSC at 150 °C was the same as for 200 °C. This indicates the overfitting problem which we were unable to solve by manual or by automated (discussed later) hyperparameter fitting with several WEKA tools.

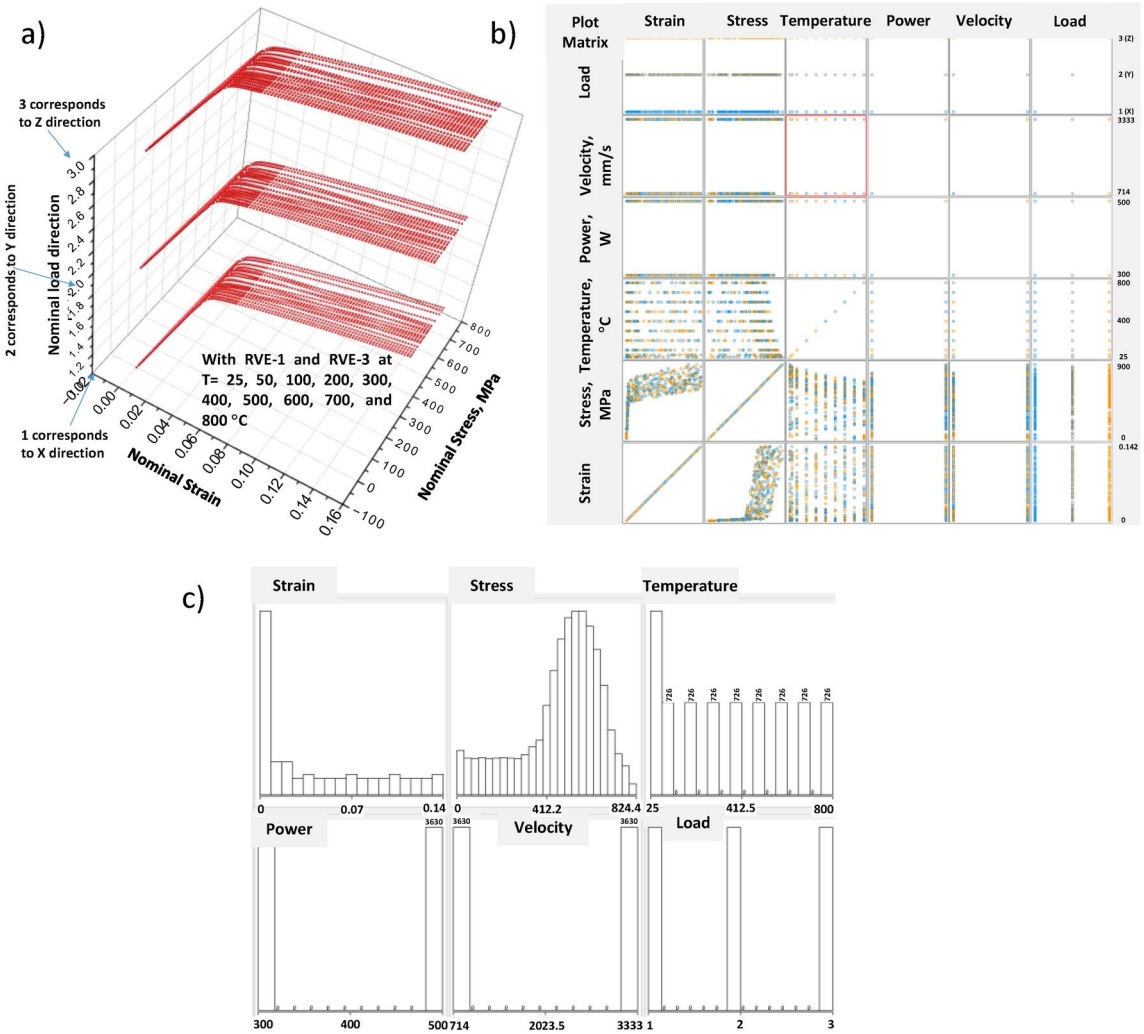

Fig. 4. Simulated SSCs for RVE-1 (E140P300v714) and RVE-3 (E50P500v3333) samples in (**a**) to test the various ML regressors with training dataset plot matrix in (**b**) and attribute statistics in (**c**).

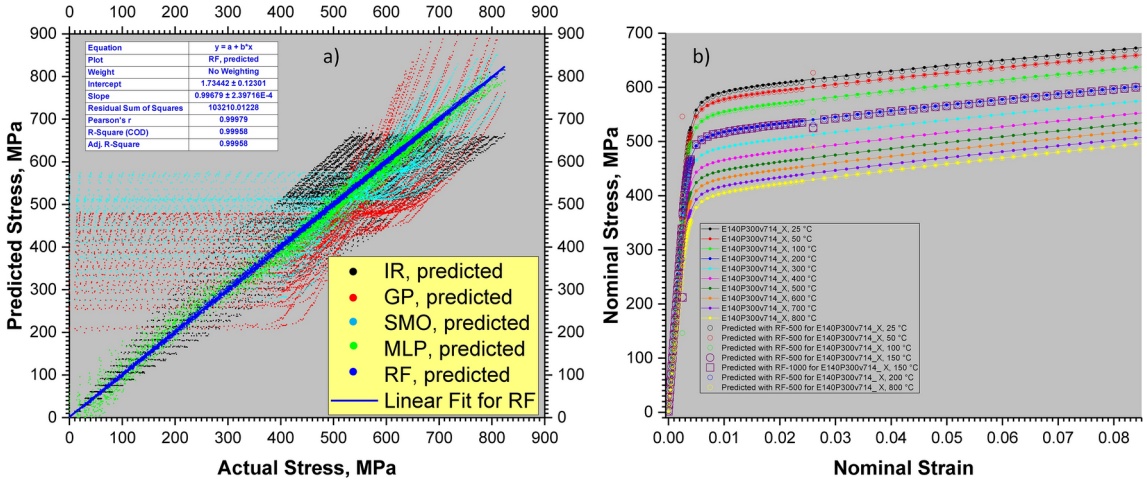

Fig. 5. In (**a**), the comparison of different ML regression models on training dataset with simulated SSC data are shown at different temperatures. In (**b**), the results are shown in more details with RF regressor, where suffixes −500, −1000 and _X are the numbers of the trees in RF and tension along x–axis, respectively. See units for other suffixes in Material and Methods.

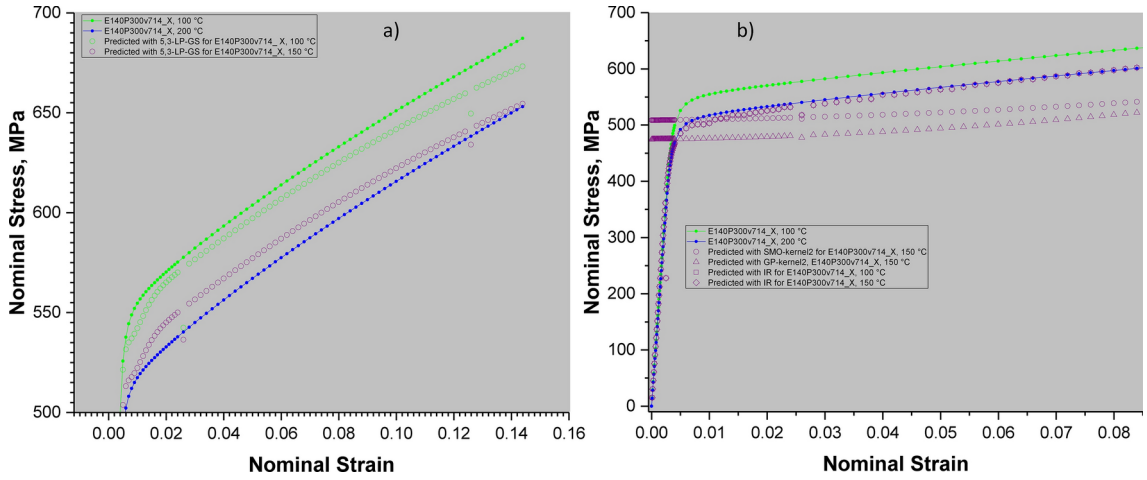

Fig. 6. Comparing of ML predicted SSCs to DAMASK simulated ones at different temperatures with MLP in (**a**) as well as with SMO, GP, and IR regressors in (**b**), where the suffixes 5,3-, kernel2 and _X are the numbers of units in hidden layers, polynomial kernel with exponent of 2 and tension along x–axis, respectively.

In the case of MLP (with backpropagation and logistic activation function), we used the WEKA GridSearch tool to find the best combination values of *momentum* (a moving average of past gradients) and *lerningRate* (gradient step size) applied to the weight updates. The number of units (the maximum value was the number of attributes) in one and two layer (sufficient for any nonlinear problem) ANN were varying manually. Some representative results are in Fig. 6a. Note that none of them demonstrates the good correspondence even with training dataset, not to mention the expected position of SSC at 150 °C. Here, it must also be stressed that the hyperparameter fitting process for this regressor the lengthy and cumbersome (not user friendly).

By using SMO and GP regressors, the SSC predictions were very bad (see Fig. 6b). In the case of SMO, it is supposed to find the optimal hyper-surface that best fits the data points while minimizing error. However, we were unable to find the reasonable SSC predictions with this regressor on our training dataset with different Kernels. With GP, the multivariate normal distribution of random variables capturing their means, variances, and correlations are indexed which provides the probabilistic predictions and incorporates the prior knowledge (kernels or covariance function). So, by using observed data and the covariance matrix, the predictive distributions are computed for unobserved points, providing both the mean prediction and uncertainty (variance). The failure of GP regressor (see Fig. 6b) was attributed to our training dataset size. There are only 2 entries with laser power and laser scan velocity as well as only 3 entries with load direction which prevent the capturing of multivariate normal distributions of random variables. The much larger training dataset is probably needed with this regressor which may not be realistic for our purpose. The results with IR, which learns an isotonic/monotonic

regression model, are also displayed on Fig. 6b. This regressor do not assumes any specific functional form, but just a smooth non-decreasing curve, so it iteratively fits a piecewise (different formulas for different segments) constant non-decreasing function to the data. Basically, the IR overfits similar to RF and has no means to solve this problem with hyperparameter optimizations.

Figure 7 shows our attempts to get SSC predictions with two decision tree regressors: M5P and alternating model trees AMT algorithms. The M5T combines a conventional single decision tree with the possibility of linear regression functions at the leaf nodes. When a prediction is required for a specific instance, the algorithm combines the decision tree path (from root to leaf) with the linear regression model at that leaf. The linear regression model provides a continuous numeric prediction based on the features of the instance. As it can be seen from Fig. 7a, the M5T gives the excellent prediction on training dataset, but still struggles for unseen SSCs at 150 and 250 °C. In contrast to all other regressors, the AMT algorithm in Fig. 7b predicts well on training dataset and quite reasonably predicts the position of unseen SSCs at 150 and 250 C. See also the results of tenfold cross-validation on training dataset with AMT in legend box.

Here it should be pointed out that AMT is a popular method for tackling regression problems requiring interpretable models[19]. Model trees are decision trees with multiple linear regression models at the leaf nodes similar to M5T. The AMT algorithm is for growing of the alternating model trees, a form of option tree for regression problems, i.e. an ensemble regressor with a single tree structure in contrast to RF[20]. As in alternating decision trees for classification, the alternating model trees for regression contain splitter and prediction nodes. Simple linear regression functions are used as opposed to constant predictors at the prediction nodes which differs from RF too (see Fig. 8a). Moreover, the greedy algorithm for additive regression by using forward stagewise modelling (iterative coefficient adjusting for minimal error) is applied to grow the tree rather than a boosting algorithm. To reduce the computational complexity and data fragmentation, the splits on numeric attributes at splitter nodes are restricted to the median value of each attribute rather than to arbitrary points indented by a split selection criterion and the size of the tree is determined by cross-validation. The empirical results show that alternating model trees achieve the significantly lower squared error than standard model trees on several regression datasets[19]. Our results also demonstrate the excellent regression capabilities for SSC predictions on our "small" training dataset compared to other tested regressors including the RF as well as the AMT user friendliness in terms of just two hyperparameters.

In Fig. 8a, the whole tree and its few branches are shown for AMT regressor on training dataset. Figure 8b demonstrates the results with AMT in more details on training dataset (black lines and symbols) and on test dataset with simulated SSCs at 150, 250, 350, 450, 550, 650, and 750 °C (red lines). The ML predicted SSC are shown with blue symbols. The typical weighted error (≅0.3%) calculated by Eq. 8 is also depicted on insert of Fig. 8b for ML predicted SSC at 150 °C ($\overline{Error}$≅0.3%):

$$\overline{Error} = \sum_{i=1}^{n} \left[\frac{\Delta\varepsilon_i}{\Delta\varepsilon} \left| 1 - \frac{SSC_{simulated}}{SSC_{machine-learned}} \right| \times 100\% \right] \tag{8}$$

where $\Delta\varepsilon_i$ and $\Delta\varepsilon$ are running and total strain intervals in SSC. The three main peaks on insert error plot were partially due to the strain sampling interval changes in DAMASK simulations which affected the ML training (see corresponding blue arrows). These sampling changes were necessary to reproduce well the SSC shape, to keep simulated files in reasonable size and to have the good convergence rate (short simulation time).

Table 4 compares the computed 0.2% proof stress (PS) values estimated from interpolations of CP simulated and ML predicted SSCs in train and test datasets. As it can be seen, almost perfect correspondence (< 2%

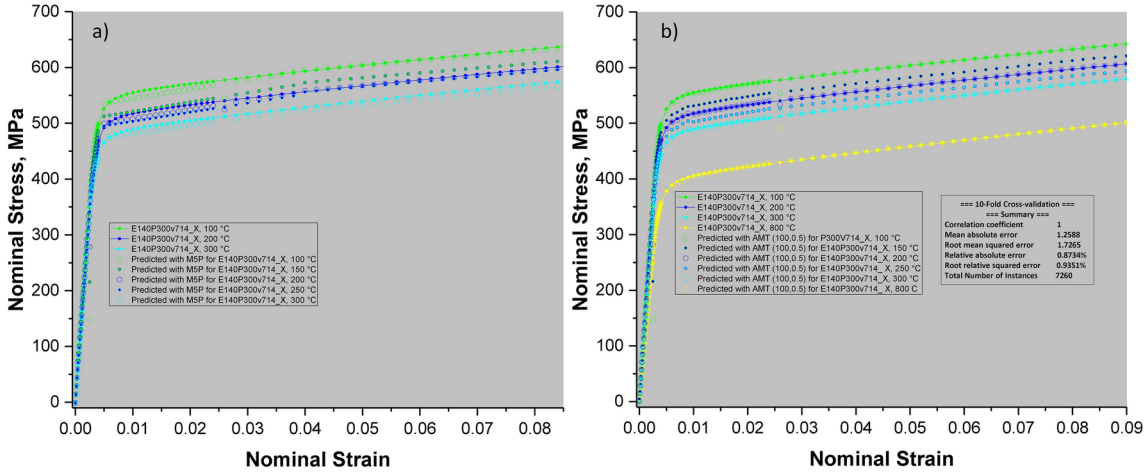

Fig. 7. Comparing of ML predicted SSCs to DAMASK simulated ones at different temperatures with M5T in (**a**) as well as with AMT regressor in (**b**), where the suffixes _X and (100, 05) indicate the tension along x–axis and (number of iterations, shrinkage), respectively.

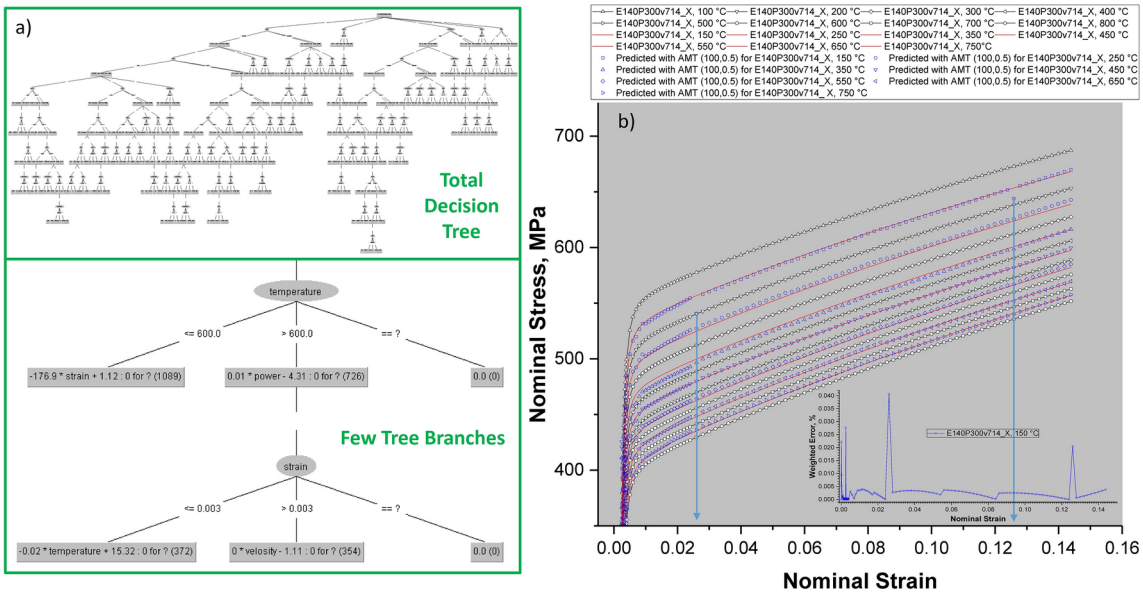

Fig. 8. Actual AMT structure after training (**a**) and comparison of AMT predicted with DAMASK simulated SSCs (**b**), i.e. the comparison with test data not used in AMT training model.

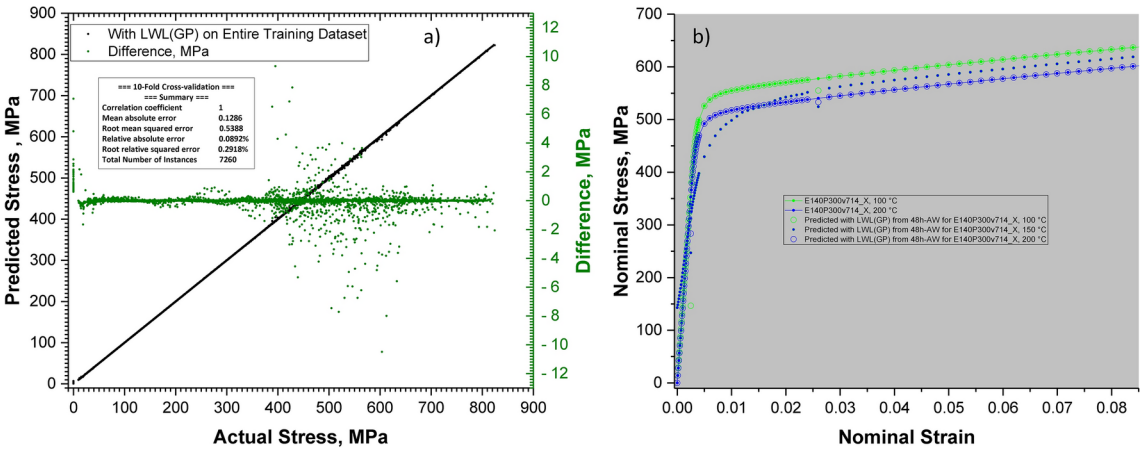

Fig. 9. (**a**) Excellent prediction results with LWL(GP) on train dataset by using hyperparameters found with AutoWEKA searched for 48 h. (**b**) Poor prediction results with LWL(GP) on test dataset by using hyperparameters found with AutoWeka searched for 48 h on train dataset (same as for (**a**)). The suffix _X indicates the tension along x–axis, see text for more details.

difference) was achieved which additionally confirms the excellent AMT algorithm performance with SSC datasets.

The ML regression for SSC predictions with AutoWEKA hyperparameter optimizations

Though we had found that AMT gave the very good regression results for predicting of SSC temperature dependences and 0.2% PS, the question was still remained on possible improvements by rigorous tuning of hyperparameters in regressors from WEKA ML package. With this aim, we also conducted several AutoWEKA runs with automatic searching through the joint space of WEKA's learning algorithms and their respective hyperparameter settings by using a state-of-the-art Bayesian optimization method with internal tenfold cross validation[21,22]. The AutoWEKA setting were to find the 4 best regressors with particular hyperparameter configurations after searches for 48 and 100 h on 32 threads of 2.9 GHz 2×CPU Worstation with 262.144 GB RAM memory allocation. As a result, the best configurations were found for GP or RF with several meta regressors.

Figure 9 shows the typical results with tuned hyperparameters. In this particular case, the best configuration of meta regressor with locally weighted learning (LWL) and GP was found by AutoWeka. Although, the perfect tenfold cross-validation results between simulated and ML predicted stress values can be achieved with tuned

hyperparameters (see Fig. 9a), the use of test dataset to predict SSC at 150 °C failed around yielding region (see Fig. 9b). In another AutoWeka run for 100 h, the meta regressor with tuned hyperparameters for additive regression (AR) and RF was found, but results were practically identical to RF in Fig. 4b, i,e. the excellent prediction of SSCs on training dataset and complete failure on test dataset due to overfitting. In some cases (not shown), the prediction of even individual SSC used in training can fail completely in spite of extremely low errors on training dataset. This means that even with such very powerful tool as AutoWEKA, which works well on many datasets including our own reported studies[23], there is no guarantee that same performance can be achieved even on same data but split differently (individual SSC predictions). With our training dataset, AutoWEKA could just output the overfitting configurations with GP, RF, and other regressors. Nevertheless, note that AutoWeka is the most comprehensive system to date compared to the Auto-sklearn or Auto-Net, for example, and can actually work extremely well with different datasets or/and classification/regression problems.

Conclusions

- In this work we demonstrated the possibility of good predictions of the entire SSC shape and position at different temperature with AMT ML algorithm by using training dataset with CP simulated SSCs based on reconstructed RVEs from experimental EBSD data and experimental SSCs of LPBF Hastelloy X material. This strategy can be applied for other industrially important materials.
- By using same PC resources, the computation time for ML-predicted SSC from well-trained classifier was 10^4–10^5 times faster compared to CP-simulated one.
- Predictions and their accuracies can be also extended and improved, respectively, on larger training datasets. Our research stresses the importance of nontrivial searching for an appropriate ML algorithm depending on training dataset structure and its size.
- The novelty of our work is in direct correspondence of LPBF experimental conditions and ML predicted SSCs.
- Besides of general curiosity, there is also an interest from the end user prospective, who is not familiar with all details of microstructure analysis, CP simulations and ML procedures. In this respect, it could be a more preferable solution in some cases compared to previously reported use of some cumbersome microstructure analysis as the necessary step before the use of expert-trained ML regressor.

Data availability

The data and datasets used and analysed in current study are available from Dr. Makoto Watanabe on reasonable request. He can be contacted through the corresponding author.

Received: 8 August 2024; Accepted: 14 November 2024
Published online: 27 November 2024

References

1. Bulgarevich, D. S., Nomoto, S., Watanabe, M. & Demura, M. Crystal plasticity simulations with representative volume element of as-build laser powder bed fusion materials. *Sci. Rep.* **13**, 20372. https://doi.org/10.1038/s41598-023-47651-2 (2023).
2. Miyazawa, Y., Briffod, F., Shiraiwa, T. & Enoki, M. Prediction of cyclic stress–strain property of steels by crystal plasticity simulations and machine learning. *Materials* **12**, 3668. https://doi.org/10.3390/ma12223668 (2019).
3. Yang, C., Kim, Y., Ryu, S. & Gua, G. X. Prediction of composite microstructure stress-strain curves using convolutional neural networks. *Mater. Des.* **189**, 108509. https://doi.org/10.1016/j.matdes.2020.108509 (2020).
4. Adachi, Y. et al. High dimensional microstructure data-driven prediction of stress-strain curve of DP steels by primary artificial intelligence. *Tetsu-to-Hagané* **102**, 47–55. https://doi.org/10.2355/tetsutohagane.TETSU-2015-069 (2016).
5. Wang, Z.-L. & Adachi, Y. Property prediction and properties-to-microstructure inverse analysis of steels by a machine-learning approach. *Mater. Sci. Eng. A* **744**, 661–670. https://doi.org/10.1016/j.msea.2018.12.049 (2019).
6. Ali, U., Muhammad, W., Brahme, A., Skiba, O. & Inal, K. Application of artificial neural networks in micromechanics for polycrystalline metals. *Int. J. Plast.* **120**, 205–219. https://doi.org/10.1016/j.ijplas.2019.05.001 (2019).
7. Nikolić, F. & Čanađija, M. Deep learning of temperature-dependent stress-strain hardening curves. *CR Mecanique* **351**, 151–170. https://doi.org/10.5802/crmeca.185 (2023).
8. Salmenjoki, H., Alava, M. J. & Laurson, L. Machine learning plastic deformation of crystals. *Nat. Commun.* **9**, 5307. https://doi.org/10.1038/s41467-018-07737-2 (2018).
9. Dorbane, A., Harrou, F., Anghel, D. C. & Sun, Y. Machine learning prediction of aluminum alloy stress–strain curves at variable temperatures with failure analysis. *J. Fail. Anal. Preven.* **24**(1), 229–244. https://doi.org/10.1007/s11668-023-01833-2 (2024).
10. Tu, Y. et al. Towards an instant structure-property prediction quality control tool for additive manufactured steel using a crystal plasticity trained deep learning surrogate. *Mater. Des.* **213**, 110345. https://doi.org/10.1016/j.matdes.2021.110345 (2022).
11. Groeber, M. A. & Jackson, M. A. DREAM.3D: a digital representation environment for the analysis of microstructure in 3D. *Integr. Mater. Manufac. Innovation* **3**(1), 56–72. https://doi.org/10.1186/2193-9772-3-5 (2014).
12. Roters, F. et al. DAMASK—the Düsseldorf advanced material simulation kit for modelling multi-physics crystal plasticity, thermal, and damage phenomena from the single crystal up to the component scale. *Comput. Mater. Sci.* **158**, 420–478. https://doi.org/10.1016/j.commatsci.2018.04.030 (2019).
13. https://damask-multiphysics.org/index.html
14. https://www.paraview.org/
15. Frank, E., Hall, M. A. & Witten, I. H. *The WEKA workbench. Online appendix for data mining: practical machine learning tools and techniques* 4th edn. (Morgan Kaufmann Burlington, 2016).
16. Sedighiani, K. et al. An efficient and robust approach to determine material parameters of crystal plasticity constitutive laws from macro-scale stress–strain curves. *Int. J. Plast.* **134**, 102779. https://doi.org/10.1016/j.ijplas.2020.102779 (2020).
17. Pilgar, C. M., Fernandez, A. M., Lucarini, S. & Segurado, J. Effect of printing direction and thickness on the mechanical behavior of SLM fabricated Hastelloy-X. *Int. J. Plast.* **153**, 103250. https://doi.org/10.1016/j.ijplas.2022.103250 (2022).
18. DAMASK—the Düsseldorf advanced material simulation kit, Spectral solver load definition, https://damask2.mpie.de/bin/view/Documentation/LoadDefinition, 2019 (accessed 1 September 2022).
19. Frank, E., Mayo, M. & Kramer, S. Alternating model trees. SAC '15: Proceedings of the 30th Annual ACM Symposium on Applied Computing. 871–878. https://doi.org/10.1145/2695664.2695848 (2015).

20. Breiman, L. Random forests. *Machine Learning.* **45**, 5–32 (2001).
21. Thornton C., *et al.* Auto-WEKA: Combined selection and hyperparameter optimization of classification algorithms. In KDD '13 *Proc. of the 19th ACM SIGKDD international conference on Knowledge discovery and data mining*; August 11–14; Chicago, Illinois: ACM New York, NY; 847–855 (2013).
22. Kotthoff, L. et al. Auto-WEKA 2.0: Automatic model selection and hyperparameter optimization in WEKA. *J. Mach. Learn Res.* **18**, 1–5 (2017).
23. Bulgarevich, D. S., Tsukamoto, S., Kasuya, T., Demura, M. & Watanabe, M. Automatic steel labelling on certain microstructural constituents with image processing and machine learning tools. *Sci. Technol. Adv. Mat.* **20**, 532–542. https://doi.org/10.1080/14686996.2019.1610668 (2019).

Acknowledgements
This work was supported by "Innovative Science and Technology Initiative for Security, Grant Number JPJ004596 implemented by the Acquisition, Technology, and Logistics Agency (ATLA), Japan".

Author contributions
D.S.B. wrote the manuscript, developed the basic concept, and performed the RVE reconstructions, CP simulations, and ML modelling. M.W. supervised this research and edited the manuscript. The manuscript was written up through contributions of all authors. All authors have given approval to the final version of the manuscript.

Competing interests
The authors declare no competing interests.

Additional information
Correspondence and requests for materials should be addressed to D.S.B.

Reprints and permissions information is available at www.nature.com/reprints.

Publisher's note Springer Nature remains neutral with regard to jurisdictional claims in published maps and institutional affiliations.